PERGAMON

Engineering Fracture Mechanics 69 (2002) 137–163

Engineering Fracture Mechanics

www.elsevier.com/locate/engfracmech

The cohesive zone model: advantages, limitations and challenges

M. Elices *, G.V. Guinea, J. Gómez, J. Planas

Universidad Politechnica de Madrid, E.T.S.I. Caminos, Ciudad Universitaria, Professor Aranguren s/n, 28040 Madrid, Spain

Abstract

This paper reviews the cohesive process zone model, a general model which can deal with the nonlinear zone ahead of the crack tip—due to plasticity or microcracking—present in many materials. Furthermore, the cohesive zone model is able to adequately predict the behaviour of uncracked structures, including those with blunt notches, and not only the response of bodies with cracks—a usual drawback of most fracture models. The cohesive zone model, originally applied to concrete and cementitious composites, can be used with success for other materials. More powerful computer programs and better knowledge of material properties may widen its potential field of application. In this paper, the cohesive zone model is shown to provide good predictions for concrete and for different notched samples of a glassy polymer (PMMA) and some steels. The paper is structured in two main sections: First, the cohesive model is reviewed and emphasis is on determination of the softening function, an essential ingredient of the cohesive model, by inverse analysis procedures. The second section is devoted to some examples of the predictive capability of the cohesive zone model when applied to different materials; concrete, PMMA and steel.

Keywords: Cohesive process zone; Concrete; Crack

1. Introduction

Linear elastic fracture mechanics (LEFM) has proven a useful tool for solving fracture problems provided a crack-like notch or flaw exists in the body and the nonlinear zone ahead of the crack tip is negligible. This is not always the case, and for ductile metals or for cementitious materials, among others, the size of the nonlinear zone—due to plasticity or microcracking—is not negligible in comparison with other dimensions of the cracked geometry. Moreover, even for brittle materials, where the process zone can be lumped into a single point, the presence of an initial crack is needed for LEFM to be applicable. This means that bodies with blunt notches—but no cracks—cannot be analysed using LEFM.

Both shortcomings are present in concrete; for ordinary concrete, the nonlinear zone, most of which coincides with the fracture process zone, can be measured in tenths of a metre and, very often, stress concentrators acting as notches can be found in structural elements. The cohesive zone model, pioneered

* Corresponding author. Tel.: +34-915-433-974; fax: +34-915-437-845.
E-mail address: melices@mater.upm.es (M. Elices).

0013-7944/02/$ - see front matter
PII: S0013-7944(01)00083-2

for concrete by Hillerborg under the name of *fictitious crack model* [23], has been used with success to surmount both difficulties. Furthermore, the cohesive model can be used as a reference frame to compare the relative abilities of the many other models dealing with concrete fracture [9]. This choice of a reference model is by no means the only possible one to compare the usual models of concrete failure, but in the cohesive model the conceptual and computational simplicity seem to be properly balanced against predictive capability and accuracy.

The cohesive process zone model is a general model which, in principle, is applicable to materials other than concrete or cementitious composites; e.g., crazing in polymers has been modelled using a cohesive surface methodology [50], and Schwalbe and collaborators modelled successfully the effect of strength mismatch in welded joints using a cohesive zone model [30]. In this paper, the cohesive zone model is shown to provide good predictions for different notched samples of PMMA and some steels. More powerful computer programs and better knowledge of material properties may widen its potential field of application.

This paper is structured in two main sections: First, the cohesive model is reviewed and emphasis is on determination of the softening function, an essential ingredient of the cohesive model, by inverse analysis procedures. The second section is devoted to some examples of the predictive capability of the cohesive zone model when applied to different materials; concrete, PMMA and steel.

2. The cohesive process zone model: background

The cohesive crack model is a suitable and simple model for the process zone, which may be viewed as a specialization of other more general approaches. For example, Broberg [4] for materials that fail by crack growth and coalescence depicts the appearance of the process zone in a cross-section normal to the crack edge as shown in Fig. 1a. He proposes to describe the process zone, in general, by decomposing it into cells. The behaviour of one single cell is defined, then, by relationships between its boundary forces and displacements. This is very similar to the definition of a finite element in computations, and when these cells are assumed to be cubic (or prismatic) and to lie along the crack path as shown in Fig. 1b, the resulting model is very similar, if not identical, to the smeared crack approach used for concrete, and, more specifically to the Bazant's crack band approach (see, e.g., Ref. [3] for a description). In fact, for a square cell of side h the relationship between stresses and displacements in the direction normal to the crack is written in Broberg's approach as

$$\sigma = \psi(\delta) \tag{1}$$

where σ and δ are, respectively, the stress and displacement normal to the crack planes. The equivalent expression for the crack band model is

$$\sigma = \psi(h\varepsilon) = \phi(\varepsilon) \tag{2}$$

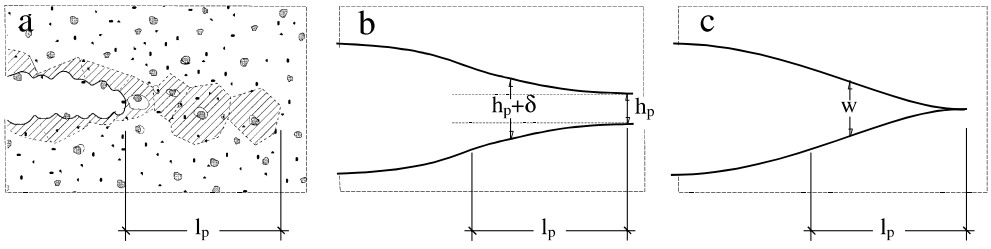

Fig. 1. (a) Sketch of the process zone (shaded area). (b) Sketch of a cohesive band process zone. (c) Sketch of a cohesive crack process zone.

where ε is the average strain in the cell (in direction normal to the crack plane). This obviously shows that Broberg's cell approach and Bazant's crack band approach are equivalent when the cells indeed form a band along the crack path (Fig. 1b). However, there are subtle differences with respect to its use in computations. The first difference is that the cell size is fixed while in the crack band the finite element size can be modified consistently. The second difference is that in the band approach, all the elements in the model reproduce the same stress–strain behaviour for the ascending part of the σ–ε curve (the hardening branch). For the cell approach, the behaviour of the material outside the process zone is that of a continuum, but its constitutive equation is not related to the behaviour of that of the cell, except for its initial slope (elastic response is the same for the cells and for the remaining part of the body).

The cohesive crack process zone (CCPZ) model can be considered as a limit of the cell model in which the cells become flat and, in the limit, they have zero width (Fig. 1c). The behaviour of the cell is equivalent, then, to an interface element in finite element methods. The behaviour of the cohesive crack is defined by the relationship between the cohesive stress and the relative displacement w between the upper and lower face of the cell (the cohesive crack width or opening):

$$\sigma = f(w) \tag{3}$$

This equation (as well as the previous equations) is strictly valid for monotonic crack opening only (or monotonic cell or band stretch). In this case, one could ask in which cases the cell or band model and the cohesive crack model are equivalent. This is developed at length in Ref. [3, Chapter 8] . The key point is that since the "cell" width is zero for the cohesive crack, the corresponding elastic displacement is also zero, as well as all the distributed displacements or strains. This implies that the cohesive crack curve (3) contains information only on the descending part of the load–displacement curve (the softening branch, called by Broberg the decohesion relation). This implies that the hardening branch in the cell or band approach must be incorporated into the behaviour of the continuum outside the cohesive zone (which we call the bulk from now on).

The correspondence between the stress–strain curves of the band (or the stress–displacement curves of the cell) and the stress–crack opening curves of the cohesive zone are illustrated in Fig. 2. For the case (very common in concrete and other quasibrittle materials) in which the hardening part is linear (which we call elastic-softening behaviour), the correspondence is simple: the bulk behaviour is linear elastic until the stress reaches the tensile strength f_t, and then softens (Fig. 2a and b). Then, given the band or cell width, there is a one to one correspondence between the fracturing strain $\varepsilon^f = \varepsilon - \sigma/E$ and the cohesive crack opening, namely $\varepsilon^f h = w$. Therefore, the equation of the softening branch in the band model (as a function of the fracturing strain) reads

$$\sigma = f(\varepsilon^f h) = \phi_s(\varepsilon^f) \tag{4}$$

The case in which there is a noticeable nonlinearity of the hardening branch in the band formulation is considerably more complex (Fig. 2c and d). As described in Ref. [3] this hardening nonlinearity must be taken up by the bulk and described through a classical stress–strain approach (Fig. 2d). The description of the softening branch is then given by an equation identical to Eq. (3), except that in this case the fracturing strain is measured from the curve corresponding to unloading from the origin, i.e.:

$$\varepsilon^f = \varepsilon - \varepsilon_u(\sigma) \tag{5}$$

where $\varepsilon_u(\sigma)$ is the strain of an element unloading from the peak point at the stress level considered.

As long as the band and cohesive crack models are linked by the foregoing relations, the resulting behaviour (as predicted, e.g., by numerical computations) is nearly the same, at least when the width h of the softening band or cell is much smaller than the dimensions of the body whose fracture is analysed.

The fact that a cohesive zone in a homogeneous body cannot have a hardening branch is sometimes overlooked. If we assume a hardening branch followed by a softening branch, as in Fig. 3, and the body is

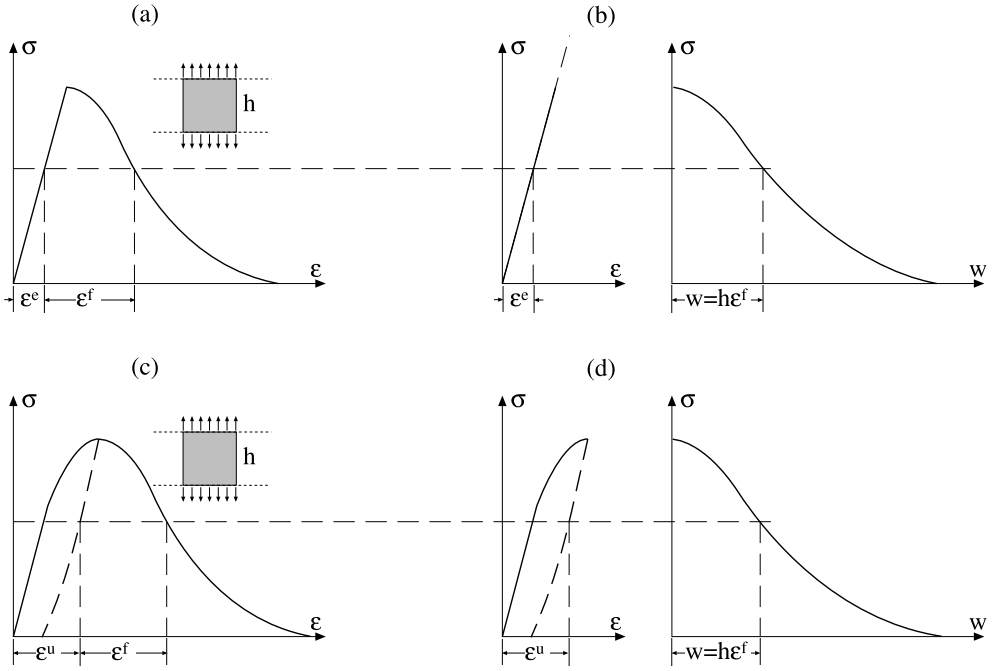

Fig. 2. Relationship between the stress–strain curves in cell or band models and the softening curve in the associate cohesive crack formulation: (a) elastic-softening band or cell model; (b) elastic-softening cohesive model; (c) general band or cell model; and (d) general cohesive model.

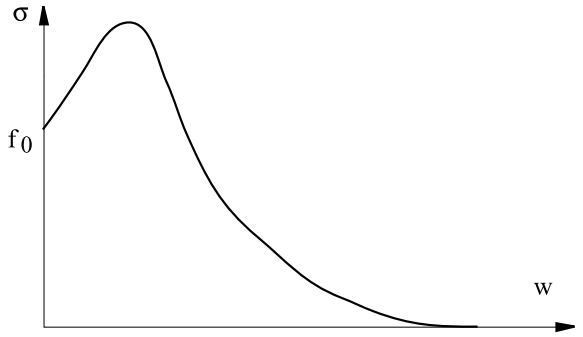

Fig. 3. Invalid cohesive stress vs. crack opening curve with a hardening branch.

initially homogeneous and isotropic, we can interpret it by saying that a cohesive crack starts to open at any given point when the stress at this point reaches f_0. Now, since the stress at this point must increase to further open the crack, this means that the stress at neighbouring points must also increase and will thus also exceed f_0, i.e., other cohesive cracks will form and start to open at neighbouring points. The resulting picture is that cohesive cracking will extend to a finite zone with infinitely close cracks with infinitely small crack openings, which means that localized cracking is in fact forbidden and what we would get by a consistent use of this model is a behaviour of the perfectly plastic type, not of the fracturing type. This means that for cohesive zones in homogeneous bodies the initial stress (the stress required for cracks to start opening) must be the absolute maximum. A monotonically decreasing function is of course a valid case, but

a function with a relative maximum less than the initial tensile strength is also acceptable. A function with a secondary maximum larger than the tensile strength would also produce an anomalous behaviour in which after a limited opening of a crack other cracks start to open in its immediate neighbourhood.

The foregoing discussion applies to homogeneous bodies in which the development of a crack is dictated by the stress distribution. A different treatment corresponds to cases where the cohesive zone grows along a pre-existing discontinuity, as for example the interface between two elastic blocks jointed by fibre bridging (stitched). In this case the stress–crack opening curve does not necessarily have to decrease because the cohesive crack (the joint) already exists and does not need to be formed. The only condition to be checked when analysing this case is that the stresses inside the blocks would not produce cracking outside the joint.

Computing mechanical behaviour of cracked structural components when the process zone is not negligible (i.e., outside the realm of LEFM), has been hampered by computing difficulties, even for the most simple model—the CCPZ model—just mentioned. These problems have been reviewed in several publications (see, e.g., Ref. [1]) and it suffices to say that two approaches were used: the boundary element method, very effective to deal with the cohesive cracks when the bulk material remains elastic (see, e.g., Ref. [44]), and the finite element method. A huge amount of computational effort has been devoted to the second approach, mainly by Ingraffea, Saouma, and Carpinteri, among others (for references, see Ref. [3]).

3. The softening function

3.1. General considerations

For cohesive crack models, the softening function $f(w)$ is considered a material property. Under mode I loading and for monotonic pure opening, the shape of the softening function for concrete is sketched in Fig. 4.

Two properties of the softening function are worth noting: the tensile strength f_t and the cohesive fracture energy G_F. The tensile strength f_t is the stress at which the crack is created and starts to open, i.e.:

$$f(0) = f_t \tag{6}$$

The cohesive fracture energy G_F is the external energy supply required to create and fully break a unit surface area of cohesive crack, and is given by the area under the softening function, i.e.,

$$G_F = \int_0^{w_c} f(w)\mathrm{d}w \tag{7}$$

where w_c is the critical crack opening, after which the cohesive stress becomes zero.

A further parameter is important for the structural behaviour, the so called characteristic length:

$$l_{ch} = \frac{EG_F}{f_t^2} \tag{8}$$

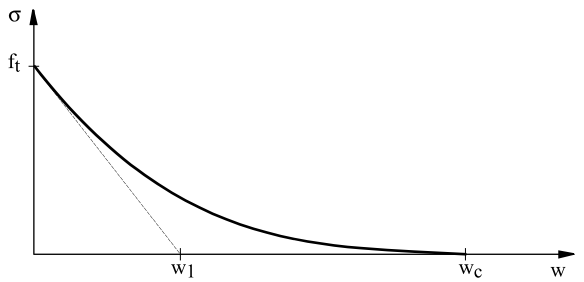

Fig. 4. Cohesive softening function and initial linear approximation.

The characteristic length is an inverse measure of the brittleness of the material (the smaller the l_{ch} the more brittle the material). It is also related to the size of the fully developed fracture process zone (the size under peak load of the fracture process zone ahead of a semi-infinite crack in an infinite body).

The softening function can be derived either from micromechanical models or from experiments. The latter has proven more useful, until now, and will be briefly reviewed in this section. Although a complete characterization of the cohesive crack model requires the full softening curve, partial information about it sometimes suffices for making predictions of engineering value. This is the case for peak load computation for very large cracked sizes and for relatively small cracked sizes:

(a) When the size of a cracked structural component is much larger than the cohesive zone size, the limit of LEFM is a reasonable first order approximation to the cohesive crack model. Under these circumstances, the peak load is fully controlled by the fracture energy G_F, irrespective of the shape of the softening function [37,39].

(b) For not too large cracked specimens and for uncracked samples, f_t and the initial slope of the softening curve become the parameters that control interesting structural properties, such as the structural strength [38,41,42]. The reason is that in such cases, the peak load occurs before any large softening occurs, i.e., at low w values, and therefore the strength is fully defined by the initial linear portion of the softening curve, which is completely defined by f_t and w_1 (see Fig. 4).

Based on the last property, a second characteristic length denoted as l_1 was introduced by the authors to describe the peak load dependence of geometrically similar bodies on their size, its expression is

$$l_1 = \frac{Ew_1}{2f_t} \tag{9}$$

The foregoing picture of the cohesive crack is, as already mentioned, the simplest version of it. There are possible extensions that are worth considering: (1) to extend the formulation so that a singularity at the cohesive crack tip is admissible (sometimes called bridged-crack model), (2) to accept a more involved behaviour, other than isotropic linear elastic, for the material outside the process zone, (3) to introduce a dependence of the softening function on constraint or triaxiality, or previous loading history and (4) to generalize the uniaxial model to a fully consistent mixed-mode formulation. Discussions of such possible extensions were published elsewhere [3,5,12]. To the author's knowledge, the third issue is one of the most frequently heard criticisms directed to the cohesive crack, but there is no basic objection to introducing a dependence of the softening curve on the triaxiality of the stress state. The last issue requires a great computational effort because the mesh is known only after the previous step has been solved, and remeshing algorithms are needed.

3.2. Experimental determination of the softening function

In principle, the most direct way to measure the softening curve is by means of stable tensile tests [33]. This kind of test seems to provide the whole σ–w curve as a direct output from the experiment, being σ and w directly measured on the specimen. However, the experimental results have shown that such an approach is extremely difficult if not impossible because of some major drawbacks:

(a) The location of the cohesive crack is not known a priori, and in most occasions multiple cracking occurs due to the material heterogeneity (Fig. 5a). This is typical of cementitious composites and ceramic materials, and has been reported even with tapered or dog bone specimens in concrete [22,34,35].

(b) For PMMA and another materials where the process zone is very small, uncracked specimens undergo large amounts of yielding before the cohesive crack forms, which increases the specimen compliance and instability. The strain energy stored in the specimen makes the test unstable even under crack opening displacement control [16,17].

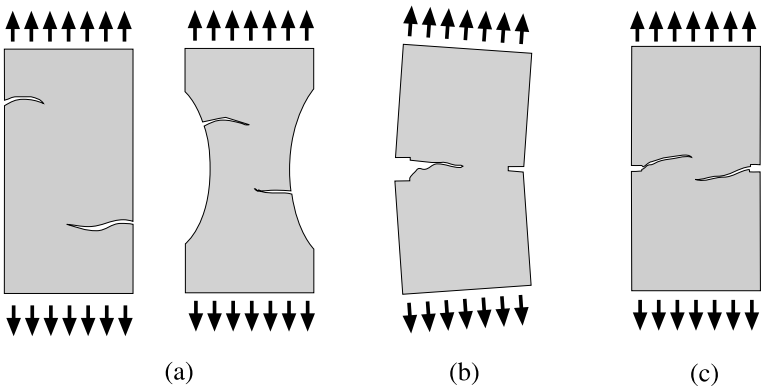

Fig. 5. (a) Multiple cracking in tensile specimens. (b) Rotation of crack faces in pre-cracked specimens. (c) Crack overlapping.

(c) When a small crack is introduced to initiate fracture and a single cohesive crack is produced, the specimen tends to asymmetric modes of fracture, and the crack opening is not uniform across the specimen, as sketched in Fig. 5b [24,49,54]. Stiffer testing machines do not solve the problem due to elastic internal rotations in the specimen itself. Moreover, when the rotations are avoided using very short specimens and a very stiff machine, or by means of special servo-controlled systems, the two cracks formed at each side of the specimen tend to get away from each other and overlap never creating a single crack (Fig. 5c) [6,54].

The inherent difficulties associated with a direct determination of the softening curve led researchers to apply indirect methods based on parametric fitting of the experimental results. These methods, known as inverse analysis or data reduction, usually do not yield identical results for the same given material due to the different weight assigned to the various experimental data. Stable tests on notched beams or compact specimens are commonly used to fit the softening curve. During the test a single crack runs in the specimen while measuring the load (P) and the displacement (δ) or the CMOD (crack mouth opening displacement).

Inverse analysis procedures are based on the simultaneous solving of a set of functional equations in the form:

$$F_1[P(\delta), \alpha_1, \alpha_2, \ldots, \alpha_N] = 0 \quad \cdots \quad F_N[P(\delta), \alpha_1, \alpha_2, \ldots, \alpha_N] = 0 \tag{10}$$

where α_i are parameters modelling the softening curve and F_j functionals of the load–displacement curve (P–δ)—or load–CMOD—for the tested geometries.

Although not explicitly stated in Eq. (10), the functionals F_j are dependent on the particular geometry of the specimen—or specimens—tested and on the assumed behaviour of the material outside the process zone.

The functionals must be selected with special care because the above set of equations tends to be ill posed. Two main groups of techniques can be distinguished regarding the selection of F_j: techniques that use the individual points (P_i, δ_i) of the load–displacement—or load–CMOD—curve for a specific test, and those that use characteristic points, or properties, of the P–δ or P–CMOD curve—e.g. the peak load, or the area under the curve—of different specimens.

Within the first group two main approaches have been published: those that use a softening curve defined a priori by N parameters α_i ($i = 1, \ldots, N$) which are best fitted by an optimization algorithm to the experimental data [31,48,52], and those that use the load–displacement—or CMOD—curve to obtain a piece-wise softening curve based on a point-to-point correspondence [25–27,51]. In this case, the parameters α_i are directly a set of points on the softening curve. These approaches have been demonstrated to be

sensitive to the optimization algorithm [52], or to give a highly unreliable initial part of the softening curve, particularly the value of the tensile strength [28]. Li et al. [29] proposed a different scheme, based on a *J*-integral technique. It is based on the subtraction of P–δ curves obtained from specimens with close notch lengths. This method, although theoretically appealing, requires very accurate and repeatable experiments, so it becomes unpractical in many instances due to insufficient accuracy.

The second group of inverse analysis techniques is based on the use of relevant points or properties of the P–δ curve in specimens with different geometry. Two different procedures were proposed by the authors depending on the relative size of the cohesive zone developed in the specimen. When the size of the process zone is of the same order of magnitude as other geometrical dimensions—as is the case of cement based materials—a simplified procedure allows the fitting of a bilinear softening curve based on the results derived from split-cylinder—Brazilian—tests and three point bend tests on pre-cracked specimens [11,20,43]. For other materials where the cohesive zone is very small—such as PMMA—a three parameter modelling of the softening curve based on the peak loads of three differently notched specimens is preferred. In both cases a linear isotropic behaviour is assumed outside the cohesive zone. These two methods are detailed in the following sections.

3.2.1. Softening curve for concrete and cement based materials

For concrete and other cementitious materials a general bilinear function as a softening function has proven very useful. This function is completely characterized by the following four parameters shown in Fig. 6: the tensile strength f_t, the specific fracture energy G_F, the abscissa of the centroid of the softening area $\bar{w}$ and the horizontal intercept w_1 of the initial linear approximation.

Two test geometries are considered; the split-cylinder or prism, and the three-point-bend pre-cracked beam. The four equations used in the method are the following:

For the split-cylinder test:

1. The size effect curve (peak load vs. specimen size)

For the three point bend test on notched beams:

2. The size effect curve.
3. The area under the complete curve of load vs. load-point displacement.
4. The far post-peak trend of the complete curve load vs. load-point displacement.

The size effect equations are computed by means of a linear approximation of the softening curve—the dashed line in Fig. 6—because, as pointed out before and shown in detail elsewhere [19,20,37,41,42], the peak load for relatively small pre-cracked specimens or for uncracked specimens of any size, happens to occur before much softening takes place anywhere in the body (i.e., for small values of w), and thus a linear

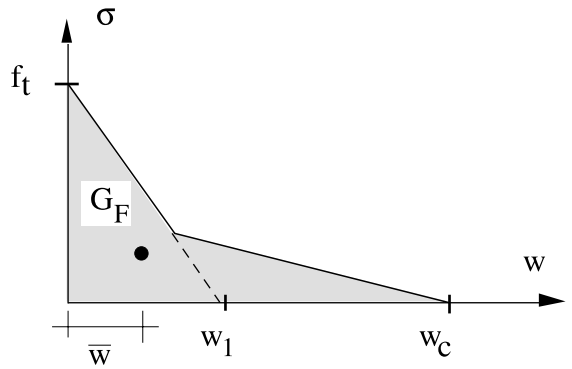

Fig. 6. General bilinear softening function. The centroid of the shaded area is marked with a dot.

approximation of the initial part of the curve suffices to describe the fracture behaviour up to and including the peak.

This property makes it possible to write the peak load for the split-cylinder test as a function of f_t and w_1 in the form:

$$\frac{2P_{uC}}{\pi D_C L_C} = f_t \phi_C \left(\frac{E' w_1}{2 D_C f_t} \right) \tag{11}$$

where P_{uC} is the peak load, L_C the length of the cylinder or prism, D_C the diameter (for cylinders) or the side of the cross-section (for square prisms), and E' the effective elastic modulus—E for plane stress and $E/(1-\nu^2)$ for plane strain. The function ϕ_C in Eq. (11) was computed numerically by the authors and shown to differ from unity by a few percent for standard test sizes [2] when the load bearing strips are thin enough [46,47]. Under these circumstances, Eq. (11) can be approximated by

$$\frac{2P_{uC}}{\pi D_C L_C} \approx f_t \tag{12}$$

and can be used to obtain a direct estimation of the tensile strength.

A similar approach can be used for the peak load of a pre-cracked (notched) beam under three point bending when the beam depth is less than $3E'w_1/2f_t$ [41,42], which is approximately 450 mm for ordinary concrete. Since laboratory specimens are commonly well under this limit, the size effect equation for a pre-cracked beam under three point bending can be expressed as a function of f_t and w_1:

$$\frac{3P_{uB}S_B}{2B_B D_B^2} = f_t \phi_B \left(\frac{E' w_1}{2 D_B f_t}, \alpha_0 \right) \tag{13}$$

where P_{uB} is the peak load, D_B and B_B are the beam depth and thickness, respectively, S_B the loading span, and α_0 the crack-to-depth ratio a_0/D_B. Again, the function ϕ_B was calculated numerically over the range of interest. For ordinary test specimens with span to depth ratio $S_B/D_B = 4$, an explicit expression has been found to solve Eq. (13) for w_1/f_t:

$$\frac{w_1}{f_t} = (1 - \alpha_0^{1.45}) \frac{D_B}{E'} \left[\frac{26.22}{(x-1)^2} + \frac{5.36}{x} \right] \tag{14}$$

where

$$x = \left[3(1-\alpha_0)^2 \frac{2 B_B D_B^2 f_t}{3 P_{uB} S_B} \right]^2 \tag{15}$$

Eq. (14) is accurate within $\pm 1.5\%$ for $0.1 \leqslant (E' w_1/2 f_t D_B) \leqslant 10$ and $0.3 \leqslant \alpha_0 \leqslant 0.7$ [43].

The combined use of Eqs. (12) and (14) suffices to determine the values of f_t and w_1 based on peak load results of split-cylinder and three point bend tests. E', the effective elastic modulus, can be determined either independently or from the initial compliance of the load–CMOD curve of the three point bend tests. As pointed out before, the knowledge of these two parameters (w_1, f_t) governing the initial linear part of the softening curve is enough in many practical situations to estimate the maximum load of ordinary structures. Nevertheless, the complete determination of the bilinear softening curve requires two further parameters: the fracture energy, G_F, and the centroid of the softening area, $\bar{w}$. To determine them, a stable three-point bend (TPB) test is needed, measuring the complete curve of load vs. load-point displacement until complete failure of the specimen. This requires that the experimental procedure takes proper care of the self-weight of the specimen, as described in Ref. [3].

The fracture energy G_F is obtained by dividing the work of fracture in three point bend tests, W, by the ligament area $B_B(D_B - a_0)$. The work of fracture W is computed by the area under the curve of load vs. load-point displacement curve (P–δ) as

$$W = \int P \, d\delta \tag{16}$$

and G_F is computed from:

$$G_F = \frac{W}{B_B(D_B - a_0)} \tag{17}$$

This is in essence the recommendation of RILEM [45] although some additional refinements are required to measure W accurately: the self-weight of the specimen must be compensated for, the sources of spurious energy dissipation must be avoided—hysteresis of the testing equipment and dissipation at the supports—and the effect of interrupting the test at a definite rotation angle has to be taken into account [10,11,18,40].

The abscissa of the centroid of the softening curve $\bar{w}$ can be evaluated from the far end of the load–load point displacement (P–δ) record for a stable three point bending test. It was shown that, under certain simplifying assumptions, this curve tends to the asymptotic form [3; 7.3.4,10,20]:

$$P \approx \frac{S_B B_B \bar{w} G_F}{4\delta^2} \tag{18}$$

Since G_F is independently determined as described above, $\bar{w}$ may be found by fitting Eq. (18) to the experimental results. Note that this requires the determination of the true far end of the P–δ curve, so that the self-weight of the specimen must be compensated.

From f_t, G_F, $\bar{w}$ and w_1, the explicit expression for the bilinear softening is the following:

$$\begin{array}{ll} \sigma = f_t(1 - w/w_1) & 0 \leqslant w \leqslant w_k \\ \sigma = \sigma_k\left(\frac{w - w_c}{w_k - w_c}\right) & w_k \leqslant w \leqslant w_c \\ \sigma = 0 & w_c \leqslant w \end{array} \tag{19}$$

where (σ_k, w_k) are the coordinates of the kink point, given by

$$w_k = w_1 \frac{w_c - 2G_F/f_t}{w_c - w_1} \quad \sigma_k = f_t \frac{2G_F/f_t - w_1}{w_c - w_1} \tag{20}$$

and w_c the critical opening, obtained from the quadratic equation:

$$w_c^2 - w_c \frac{6\bar{w}G_F/f_t - 2w_1 G_F/f_t}{2G_F/f_t - w_1} + \frac{6\bar{w}w_1 G_F/f_t - 4w_1(G_F/f_t)^2}{2G_F/f_t - w_1} = 0 \tag{21}$$

3.2.2. Softening curve for polymethyl-methacrylate

Polymethyl-methacrylate (PMMA) is an amorphous glassy polymer that exhibits brittle fracture when tested with cracks or sharp notches. The cohesive zone at the crack tip is typically not larger that a few tenths of a millimetre, and the softening function can be approximated by a truncated linear function, Fig. 7 [16,17] given by

$$\begin{array}{ll} \sigma = f_t(1 - w/w_1) & 0 \leqslant w \leqslant w_c \\ \sigma = 0 & w_c \leqslant w \end{array} \tag{22}$$

The softening function is characterized by three parameters: the tensile strength f_t, the specific fracture energy G_F, and the horizontal intercept w_1 of the initial linear approximation. The critical crack opening, w_c, is readily obtained as a function of f_t, G_F and w_1 as

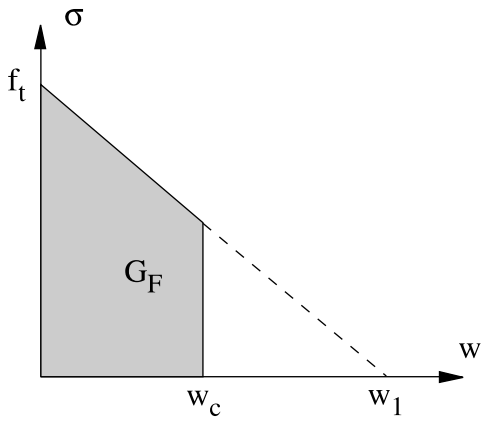

Fig. 7. Softening function dependent on three parameters.

$$w_c = w_1\left[1 - \sqrt{1 - \frac{2G_F}{f_t w_1}}\right] \tag{23}$$

The three parameters can be obtained from the size effect curve for three test geometries: the pre-cracked three point bending beam and the two differently U-notched three point bending beams sketched in Fig. 8.

The size effect equations for the two notched beams ($R/D = 0.07$ and 0.0048) is computed with a linear approximation of the softening curve, as mentioned in the previous section, because for notched geometries only the initial part of the softening curve is relevant. Similar to the analysis for concrete specimens, the peak load for beams of given geometry takes the form:

$$\frac{6P_u}{BD} = f_t\phi(D^*) \tag{24}$$

where P_u is the peak load, D and B are the beam depth and thickness (Fig. 8), and D^* the dimensionless beam depth defined as

$$D^* = \frac{2Df_t}{E'w_1} \tag{25}$$

The function $\phi(D^*)$ can be computed for each geometry over the range of interest. The resulting expressions for the geometry shown in Fig. 8 and $R/D = 0.07$ and 0.0048 are as follows:

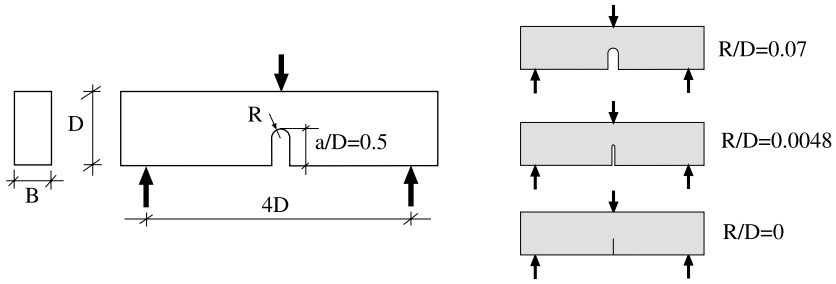

Fig. 8. Test geometries for determining the softening curve in PMMA.

For $R/D = 0.07$

$$\frac{6P_u}{BD} = f_t \frac{1 + 0.16D^*}{1 + 1.4D^*} \tag{26}$$

For $R/D = 0.0048$

$$\frac{6P_u}{BD} = f_t \frac{1 + 0.011D^*}{1 + 0.35D^*} \tag{27}$$

For the range of interest $100 \leqslant D^* \leqslant 2000$, Eqs. (26) and (27) are within $\pm 1\%$ error ($D^* \approx 300$ for a beam made of PMMA with $D = 30$ mm).

LEFM is used to obtain the size effect equation for the pre-cracked beams, taking into account that the size of the cohesive zone relative to the other dimensions of the beam (including the crack) is negligible. The authors have shown that in this situation the cohesive crack model tends to LEFM theory, and that the fracture energy G_F converges to LEFM's critical energy release rate G_c [36,38]. Therefore, G_F is obtained from the stress intensity factor at peak load, K_{IC}, through Irwin's equation:

$$G_F = \frac{K_{IC}^2}{E'} \tag{28}$$

where K_{IC} can be estimated for a beam under three point bending according to [21]:

$$K_{IC} = \frac{3P_u}{2B\sqrt{D}} \frac{\sqrt{\alpha}}{(1-\alpha)^{3/2}(1+3\alpha)} [\beta p_1(\alpha) + 4p_2(\alpha)] \tag{29}$$

where P_u is the peak load, $\beta = S/D$ and $\alpha = a/D$ the span and crack-to-depth ratios, respectively (see Fig. 8), and p_i the following polynomials:

$$p_1(\alpha) = 1.99 + 0.83\alpha - 0.31\alpha^2 + 0.14\alpha^3 \tag{30}$$

$$p_2(\alpha) = 0.09 + 0.42\alpha - 0.82\alpha^2 + 0.31\alpha^3 \tag{31}$$

These expressions are valid for any α and for $\beta \geqslant 2.5$ within a 0.5% error.

From the three Eqs. (26)–(28) the parameters f_t, w_1 and G_F can be computed, and consequently, the softening curve (22) is completely known. However, two final requirements must be checked to ensure that Eqs. (26) and (27) were properly used, and that at peak load no point on the cohesive crack in the U-notched beams has softened further than w_c. Once computed by means of Eqs. (26)–(28), the values of G_F, f_t and w_1 must fulfil the following two conditions:

$$G_F \geqslant \frac{f_t w_1}{2} \frac{349 + D^*}{807 + D^{*1.6}} \tag{32}$$

and

$$G_F \geqslant \frac{f_t w_1}{2} \frac{3646 + D^*}{3200 + D^{*1.4}} \tag{33}$$

where D^* is the nondimensional depth given by Eq. (25).

4. Experimental validation of the cohesive model

The cohesive process zone model can be applied, in principle, to any material provided fracture is dominated by tensile stresses. The aim of this section is to show some examples of its applicability not only to concrete, but to PMMA and to some kinds of steel.

It is worth noting that in all cases the softening function was obtained through *independent* tests and from this information the load–displacement behaviour and peak loads were computed and checked with experiments done with samples of *different geometry* and *size*.

4.1. Concrete

Concrete is a *quasibrittle* material, a term recently coined to identify materials that show small plastic (irrecoverable) deformation after full fracture but exhibit a relatively large cohesive process zone ahead of a pre-existing macrocrack where the interdependence of stresses and strains is nonlinear. The nonlinear zone ahead of the crack tip is very large compared to usual specimen (or structure) dimensions. This rules out LEFM because the nonlinear zone cannot be neglected.

The cohesive crack model appears as a simple method of modelling the fracture of plain concrete specimens, with very good agreement with experiments. The following examples show how this model not only predicts accurately the maximum loads for different geometries and sizes but also is able to make reasonably good predictions of load and displacements at any instant throughout the test, even for unnotched specimens.

4.1.1. Concrete under mode I loading

When measuring the tensile strength of concrete by means of flexure tests it appears that its value is higher than that obtained through direct tension tests [32]. In addition, it is observed that the flexural tensile strength is dependent on the size of the beam tested.

Such size effect can be evaluated with an empirical expression that relates both tensile strengths (flexural and axial) to beam size, given by Ref. [7]

$$f_t = f_{t,fl}\frac{2.0(D/D_0)^{0.7}}{1+2.0(D/D_0)^{0.7}} \tag{34}$$

where f_t is the tensile strength, $f_{t,fl}$ the mean value of flexural tensile strength, D the beam depth and D_0 is a reference size equal to 100 mm. This expression is applicable to beam depths of more than 50 mm.

This empirical expression was used for checking the predictive properties of the cohesive process zone model. To this end, concrete beams of different sizes were tested and the flexural tensile strength was measured and compared with the cohesive model predictions. Details of concrete manufacture and storage are given in Ref. [35]. The maximum aggregate size was 16 mm, the specimens were stored in lime saturated water and the tests were performed with special care to avoid shrinkage during the preparation of the specimens.

Table 1 shows the mechanical properties of the concrete: elastic modulus, compressive strength and splitting tensile strength, measured according to ASTM C-469, ASTM C-39 and ASTM C-496, respectively. The tensile strength f_t was estimated as equal to the splitting tensile strength f_{st}, as commented in Section 3.2.

To measure the flexural strength, stable TPB tests on unnotched beams were performed using full weight-compensation. Two sets of beams were tested with a span to depth ratio of 4 and depths of 30 and 96 mm. The thickness was 100 mm for all the beams. The values obtained for the flexural tensile strength are plotted in Fig. 9, where the ordinates are made nondimensional by dividing them by f_t.

Table 1
Mechanical properties of the concrete

E (GPa)	f_c (MPa)	f_t (MPa)
39 ± 1	48.5 ± 0.4	3.9 ± 0.2

Errors correspond to 95% confidence interval.

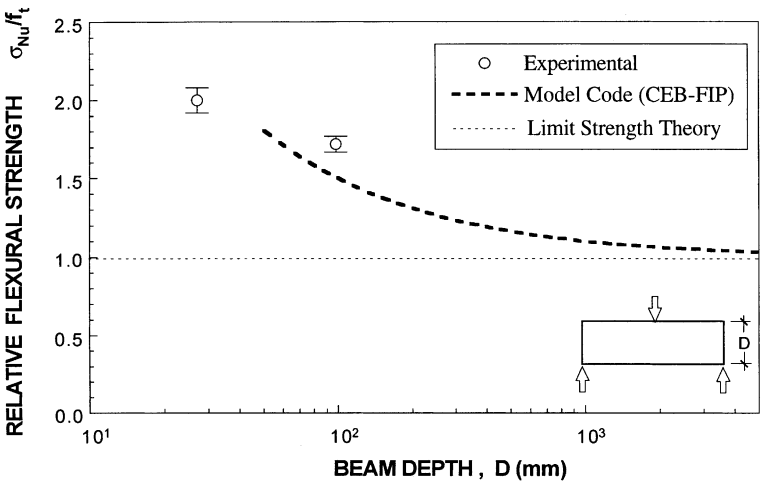

Fig. 9. Size effect in maximum load for unnotched beams. $\sigma_{Nu} = 6P_u/BD$; P_u = ultimate load, B = thickness, D = beam depth.

Table 2
Fracture properties of the concrete

E (GPa)	f_t (MPa)	G_F (J/m^2)	w_1 (μm)	$\bar{w}$ (μm)
39 ± 1	3.9 ± 0.2	126 ± 14	53 ± 9	42 ± 9

Figures are mean values and standard error, with 95% confidence.

As shown in the figure, experimental results display the same trend as the empirical equation of the model code, a result unobtainable from the limit analysis theory.

A prediction of the size effect was made to check the suitability of the fracture process cohesive model. The four parameters that define a bilinear softening curve, needed for numerical computations, were obtained according to the method described in Section 3.2.1, and the results are given in Table 2. In particular G_F, w_1 and $\bar{w}$ were determined from tests on notched beams cast from the same batch. As outputs, peak load, load–CMOD and load–displacement curves were obtained for the two series of unnotched beams.

Fig. 10 shows the numerical prediction of the size effect at peak load. The agreement with experimental results deserves some comments: The experimental point for *notched* beams is the reference point from which *all* information was derived (i.e. the softening curve) and the prediction of the cohesive model should cross through this point, as it does. The encouraging result is the very good agreement for *unnotched* beams of the two sizes, particularly if it is realized that the two geometries—notched and unnotched—are quite different.

Fig. 11 shows the comparison of the predicted loads and horizontal displacements at midspan with the measured ones for the unnotched beams. One may conclude that the prediction obtained using a cohesive crack model with a softening curve (determined from *independent* tests on *notched* beams), is very good, particularly if one realizes that predictions are for *unnotched* specimens.

4.1.2. Concrete under mixed mode loading

The local cohesive process zone model is also a useful tool to analyse mixed mode (I/II) fracture of concrete. As an example, the results of two set of mixed mode tests performed by the authors are briefly commented. Details of the experiments and the numerical simulation can be found elsewhere [8,14,15].

Two set of tests, under *proportional* and *nonproportional* mixed mode loading, were performed on notched beams in bending. Fig. 12 shows the geometry, forces and boundary conditions of the tests. Type 1

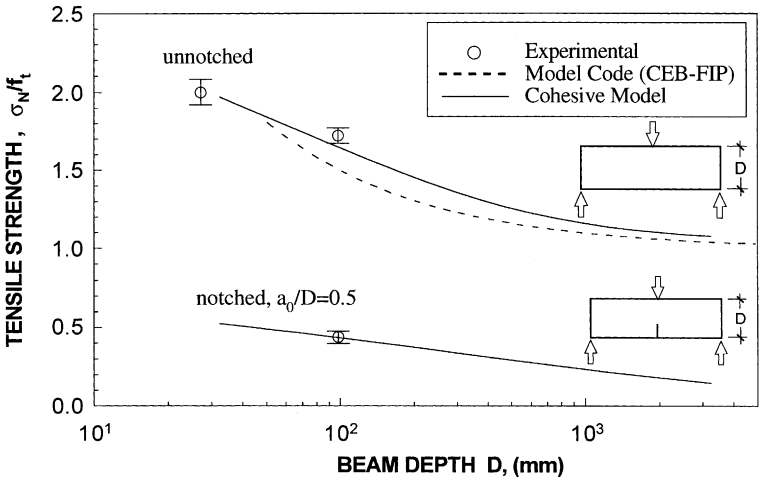

Fig. 10. Maximum load size-effect for three point bend beams notched and unnotched. $\sigma_{Nu} = 6P_u/BD$; P_u = ultimate load, B = thickness, D = beam depth.

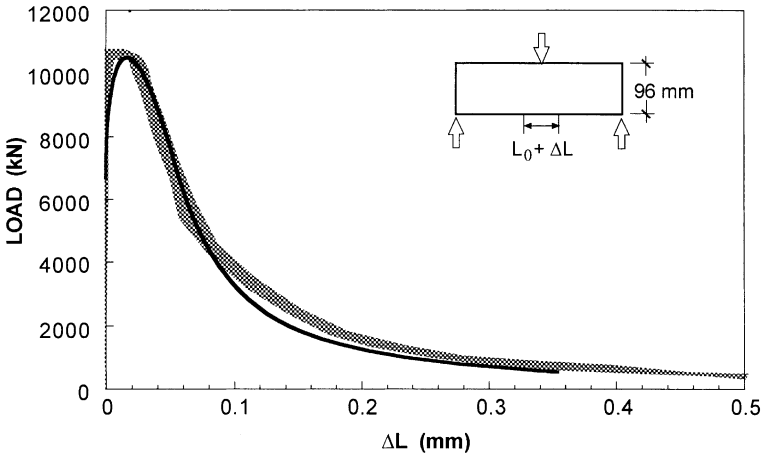

Fig. 11. Results of tests on unnotched specimens (shaded) compared with the cohesive crack model prediction based on notched specimens (solid line). Gauge length, $L_0 = 25$ mm, beam thickness = 100 mm, loading span = 384 mm.

test corresponds to a free displacement condition of point B ($K = 0$), where no load is applied. In type 2 test, the displacement of B is prevented ($K = \infty$), resulting in the application of a nonproportional load at this point. The beams are asymmetrically loaded to force the crack to propagate under mixed mode.

Three sizes of geometrically similar beams were tested (actually, the beams were not exactly similar because it was impossible to fully scale down the loading devices, but they were very close to similar). The standard mechanical properties were measured according to ASTM, and are given in Table 3. Fracture properties, in particular those defining a bilinear softening curve, were determined from the procedure outlined in Section 3.2.1. Values of the tensile strength f_t, the fracture energy G_F, the horizontal intercept of the initial part of the softening curve w_1, and the position of the centroid $\bar{w}$ were independently measured in three point bend and cylinder splitting tests, and are also given in Table 3.

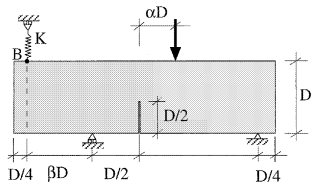

Type 1 : K=0
Type 2 : K=∞

D(mm)	α	β
75	1.13	1.50
150	1.0	1.50
300	1.0	1.33

Fig. 12. Geometry, forces and boundary conditions in mixed mode tests.

Table 3
Properties of the concrete for mixed mode tests

E (GPa)	f_c (MPa)	G_F (J/m^2)	f_t (MPa)	$\bar{w}$ (μm)	w_1 (μm)
38.4 ± 0.5	57 ± 2	69 ± 4	3.0 ± 0.1	36.0	24.1

Errors correspond to 95% confidence interval.

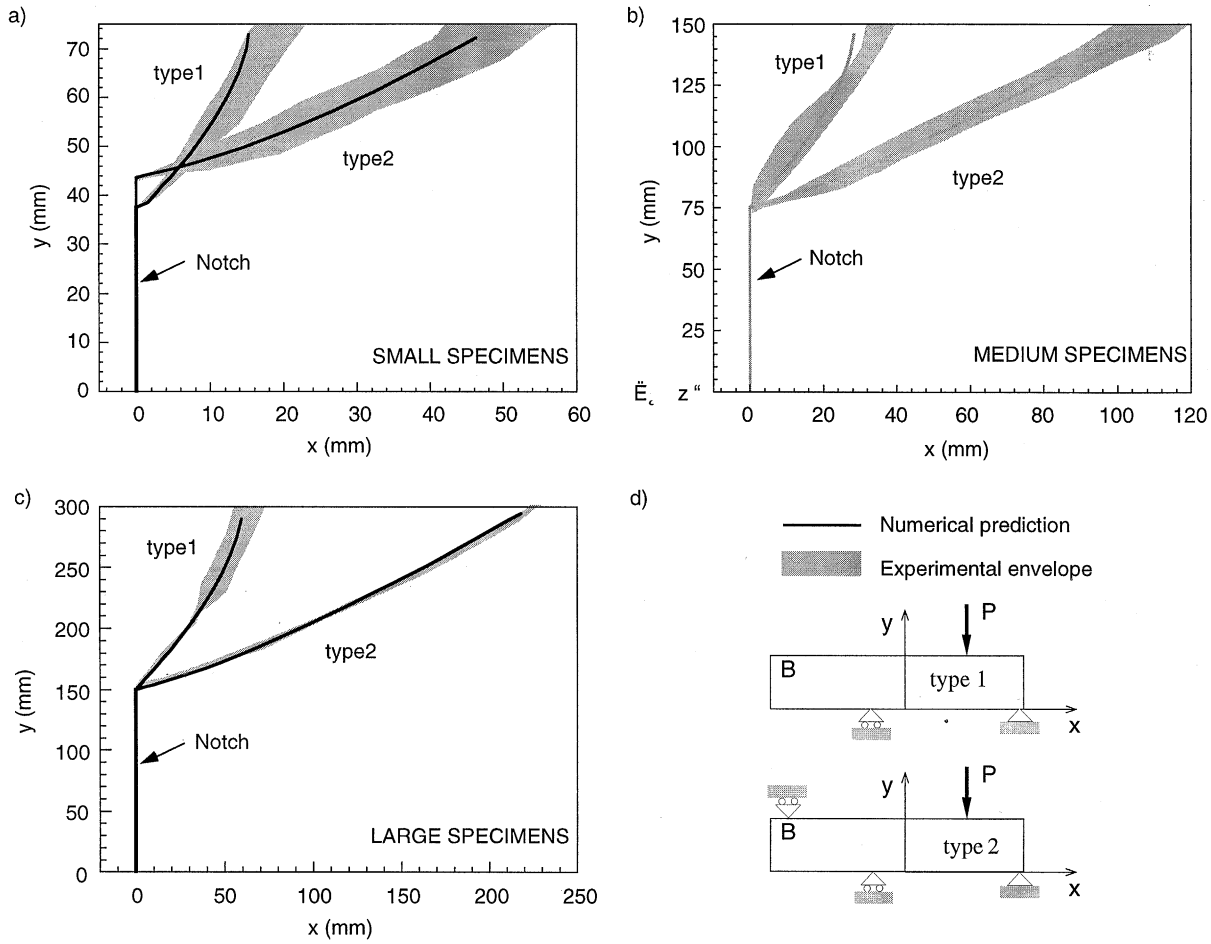

Fig. 13. Crack trajectories for mixed mode test. (a) Specimens with $D = 75$ mm. (b) Specimens with $D = 150$ mm. (c) Specimens with $D = 300$ mm (from Ref. [13]).

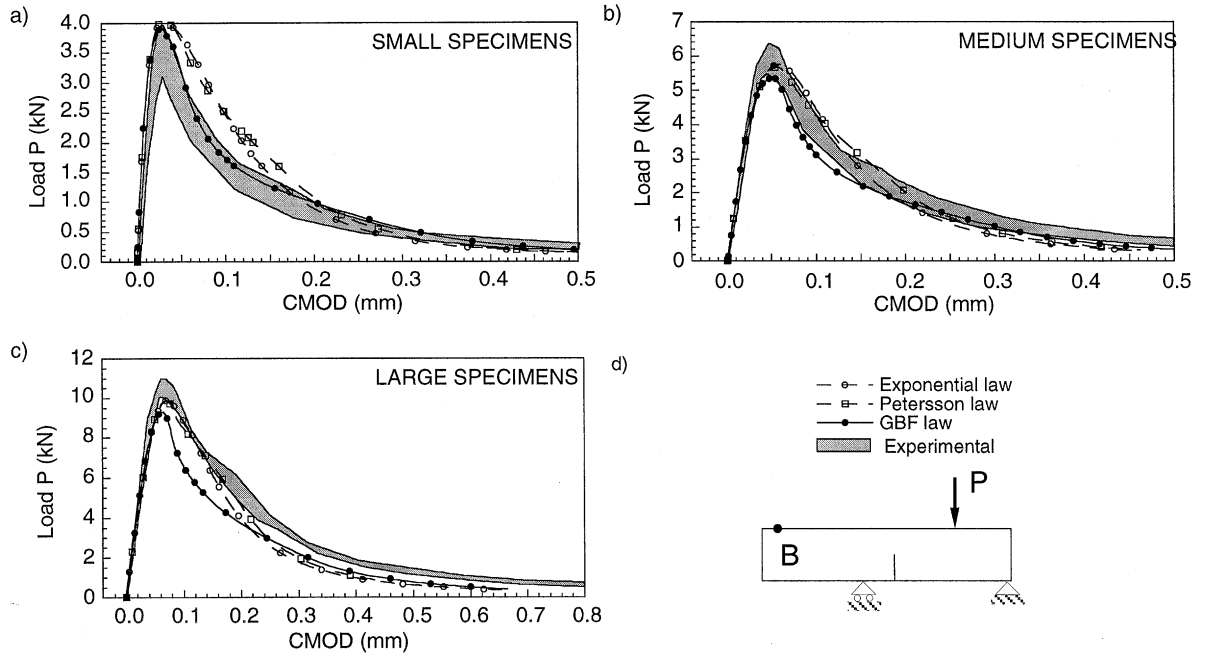

Fig. 14. Load–CMOD curves: experimental results and numerical predictions for type 1 tests. (a) Specimens with $D = 75$ mm. (b) Specimens with $D = 150$ mm. (c) Specimens with $D = 300$ mm (from Ref. [8]).

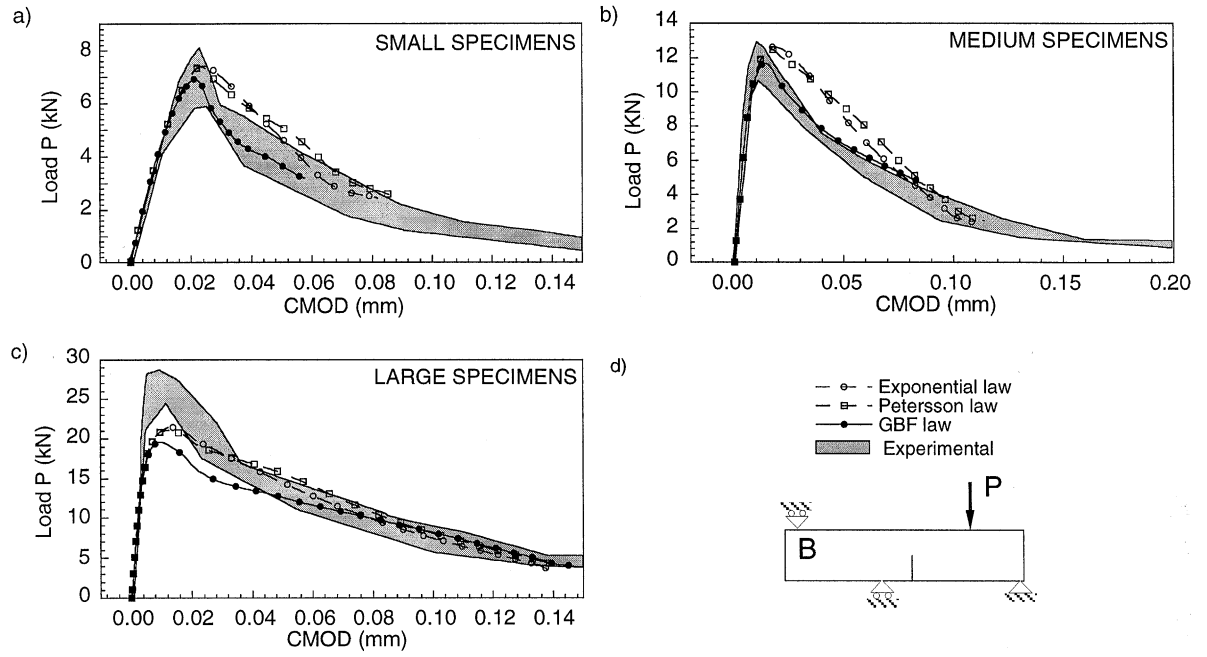

Fig. 15. Load–CMOD curves: experimental results and numerical predictions for type 2 tests. (a) Specimens with $D = 75$ mm. (b) Specimens with $D = 150$ mm. (c) Specimens with $D = 300$ mm (from Ref. [8]).

The numerical simulation is based on the incorporation of the cohesive crack model into a finite element code. This is performed: (1) using LEFM to predict the crack path, which gives a reasonable estimate, even for involved trajectories [13]; and (2) incorporating the cohesive model into the crack path by means of nonlinear springs [8], and assuming that the crack grows in a stable manner in local mode I. One hundred two-node nonlinear springs following the stress–displacement relationship given by the softening curve were placed along the computed crack path. The material outside the cohesive zone was assumed to behave linear-elastically.

Fig. 13 shows the experimental envelopes and the numerical prediction of the crack paths for the two types of test and the three specimen sizes. The accuracy of the numerical predictions gives further support to the hypothesis that the elastic crack path is a good estimate of the actual crack path for concrete structures.

Figs. 14 and 15 compare the load–CMOD curves recorded in the experiments with the predictions using the cohesive process zone crack model. The numerical predictions are, once again, very accurate, even more if it is considered that they are actual *predictions*, based on an independent set of tests in mode I. The results show the ability of the cohesive crack model to cope with mixed mode problems and, more importantly, to produce accurate results based only on material properties measured by standardized methods. In addition, the cohesive crack model can be easily implemented with general multipurpose finite element codes.

4.2. Polymethyl-methacrylate

The CCPZ model can also be applied to materials other than concrete and cementitious composites. This section shows an example where this model predicts accurately peak loads and load–displacement curves for notched—not cracked—polymer samples.

The material chosen for the experimental program was the amorphous glassy polymer polymethyl-methacrylate (PMMA). From tensile tests, at a strain rate of 0.00014 s^{-1} and at room temperature, the following average values were obtained: Young modulus $E = 300 \pm 30$ MPa, yield limit stress $\sigma_{0,2} = 43.9 \pm 0.7$ MPa, rupture stress $\sigma_R = 74.9 \pm 0.2$ MPa and Poisson's ratio $v = 0.4$. A representative stress–strain curve is shown in Fig. 16.

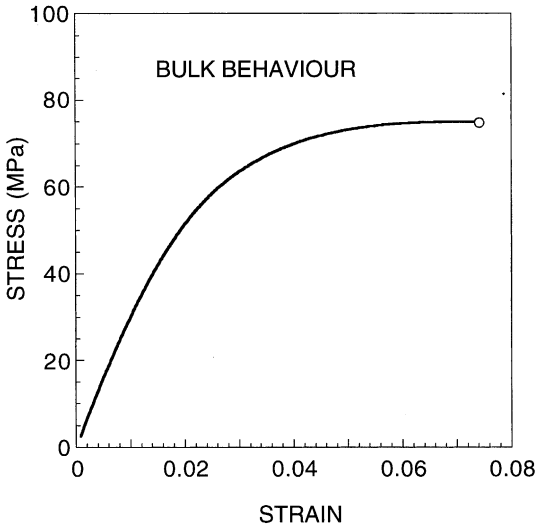

Fig. 16. Stress–strain curve for PMMA.

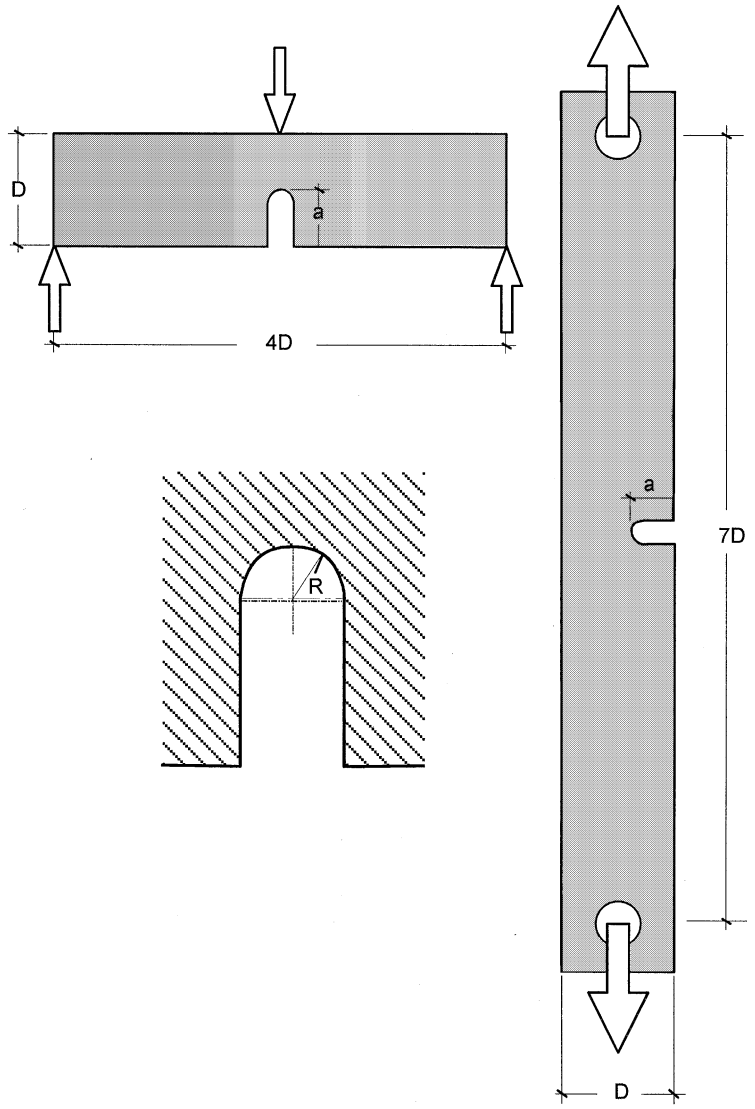

Fig. 17. Geometry of notched specimens of PMMA (thickness in all specimens was 14 mm).

Two types of specimens were tested; TPB beams and single-edge-notched (SEN) tensile specimens. Both were selected for their simplicity and are shown in Fig. 17 with the loading mode and geometrical notation. In all specimens, the thickness was 14 mm.

Experimental results of load vs. notch-mouth opening displacement (NOD) are shown in Fig. 18. All tests were performed under NOD control and at room temperature. A minimum of four samples was tested for each configuration.

Numerical predictions of load–NOD curves and peak loads were performed using the CCPZ model. In this respect, it is worth emphasizing that *all* numerical predictions are based only on the same two parameters (σ_R and G_F), which were measured through two independent tests. The softening function, the main input for the CCPZ model, was obtained by the indirect procedure, given the small characteristic

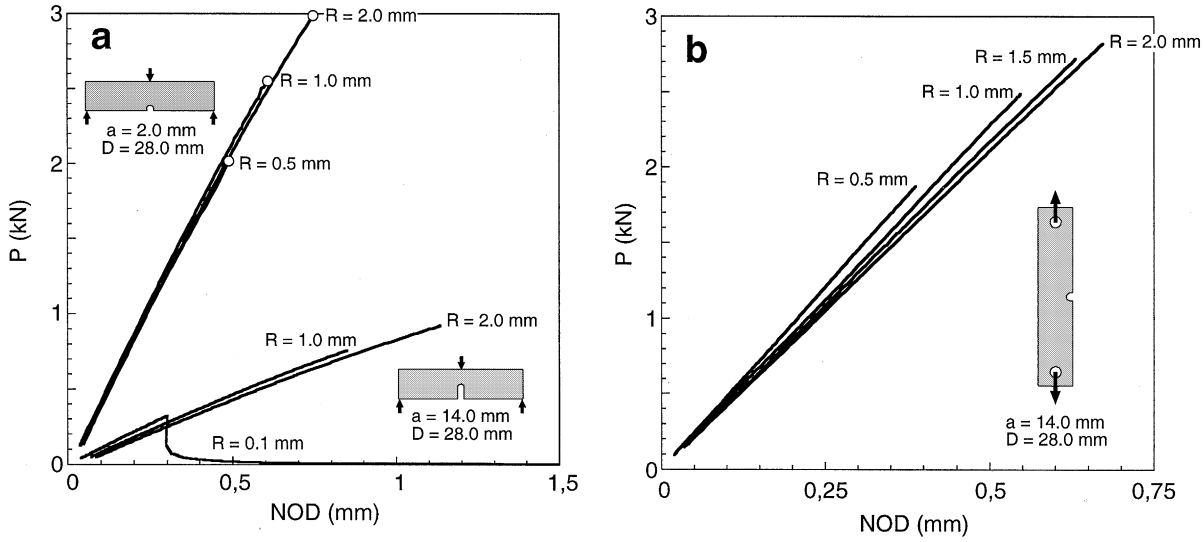

Fig. 18. Load vs. NOD curves: experimental results for PMMA performed under NOD control.

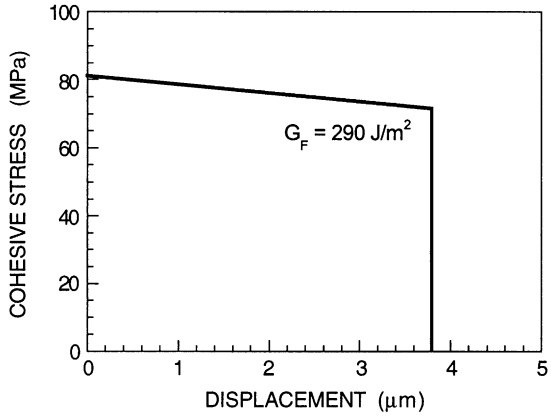

Fig. 19. Softening function for PMMA.

length, of about 0.015 mm. For such values, machining suitable samples for the direct method was impractical. The needed value of the specific fracture energy G_F was measured from four tests with precracked TPB beams, 14 mm thick and 28 mm wide, according to ASTM 813 standard. The softening function used for PMMA is depicted in Fig. 19. The material outside the process zone was modelled as a nonlinear elastic material, following the stress–strain relation depicted in Fig. 16, with a constant Poisson's ratio of 0.4.

The numerical predictions of load–NOD curves give nearly straight lines, in good agreement with experimental measures depicted in Fig. 18. For the peak loads, Fig. 20 compares the peak loads derived from experimental results and numerical predictions. The range of the experimental results for each notch radius is represented by a bar and the average value by an open circle. Numerical values are shown as full lines; to account for small differences in notch length, when machining the notch, a band embracing two limiting realistic values was computed for each geometry (values of notch lengths a are shown in the figure). The agreement is very good. Furthermore, when the radius decreases (when the notch becomes a crack), ex-

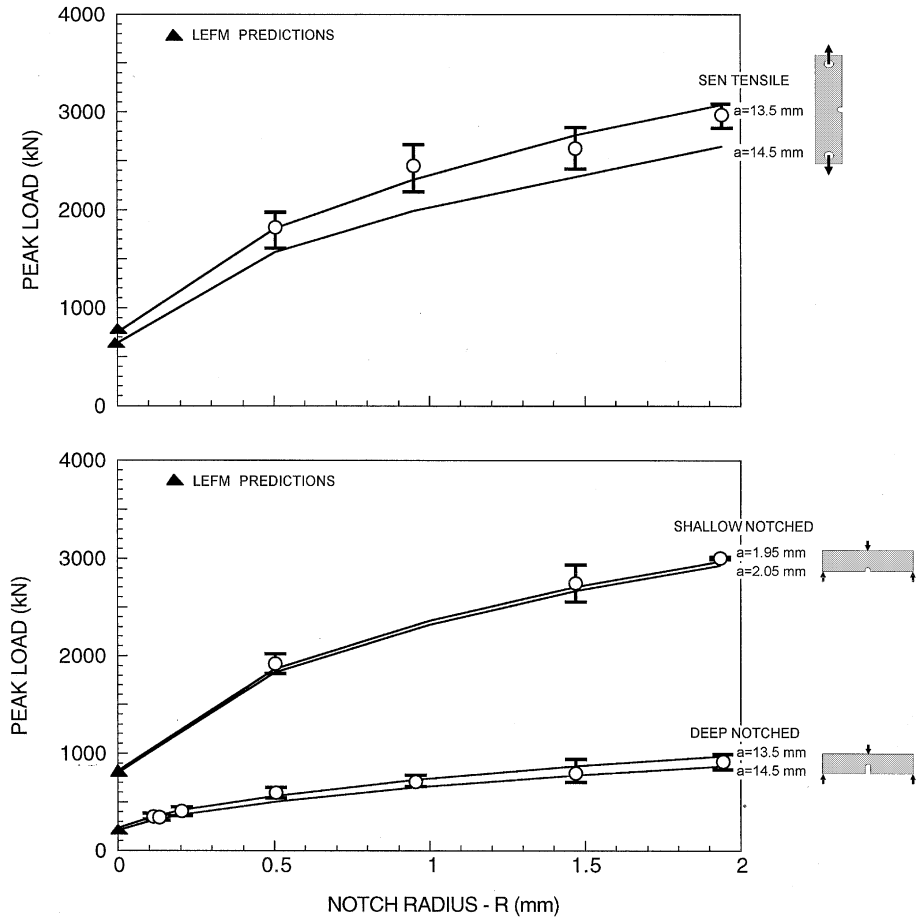

Fig. 20. Numerical predictions and experimental results of peak loads for TPB and SEN notched specimens of PMMA.

perimental results and numerical predictions converge to the simple analytical predictions of LEFM with $K_{IC} = (EG_F)^{1/2} \approx 1$ MPa m$^{1/2}$. These results are shown in the vertical axis of Fig. 20 (full triangles).

4.3. Steel

Modelling the process zone as a cohesive crack has also been successful for some kinds of steel. The example shown here allowed computation of load–displacement curves and prediction of peak loads for "notched" (not cracked) steel samples of different geometries and sizes. Notice that these computations could not be done using fracture mechanics because no initial cracks were present.

Steel samples were from a pearlitic steel, hot rolled and air cooled. The average size of pearlite colonies was about 10 μm. Chemical composition is shown in Table 4.

Table 4
Steel chemical composition

Element	C	Si	Mn	P	S	V
Weight %	0.65	0.70	1.20	0.014	0.018	0.25

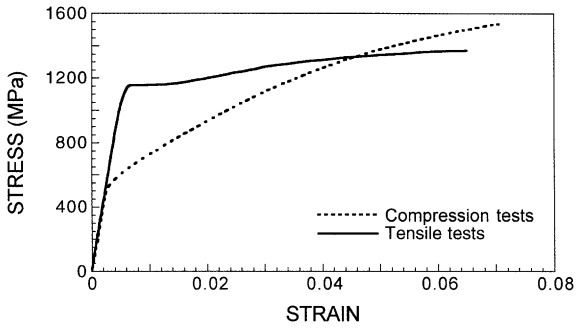

Fig. 21. Stress–strain curve for a hot rolled pearlitic steel.

Mechanical behaviour was quite different when tested under tensile or compressive loads, as shown in Fig. 21. From these tests the following mechanical parameters were inferred: elastic modulus = 208 GPa, tensile yield stress = 1143 MPa, compressive yield stress = 625 MPa, ultimate tensile stress = 1350 MPa, average elongation under maximum tensile load = 7%.

Fracture toughness for crack propagation normal to the rolling direction was measured from cracked beams, according to ASTM E399 standard, and from short bar specimens, according to ASTM E1304 standard. Details of these measurements were published elsewhere [53]. The measured value was 33 MPa $m^{1/2}$.

To check the suitability of the CCPZ model, three types of notched—not cracked—specimens were tested: deep notched beams (with nominal notch radii of 0.1, 0.2, 0.5 and 1 mm), shallow notched beams (with nominal notch radii of 0.1, 0.2 and 0.5 mm) and Charpy V notched beams. The geometry and dimensions of the samples are shown in Fig. 22. Actual values of notch depth and radii are given in Table 5.

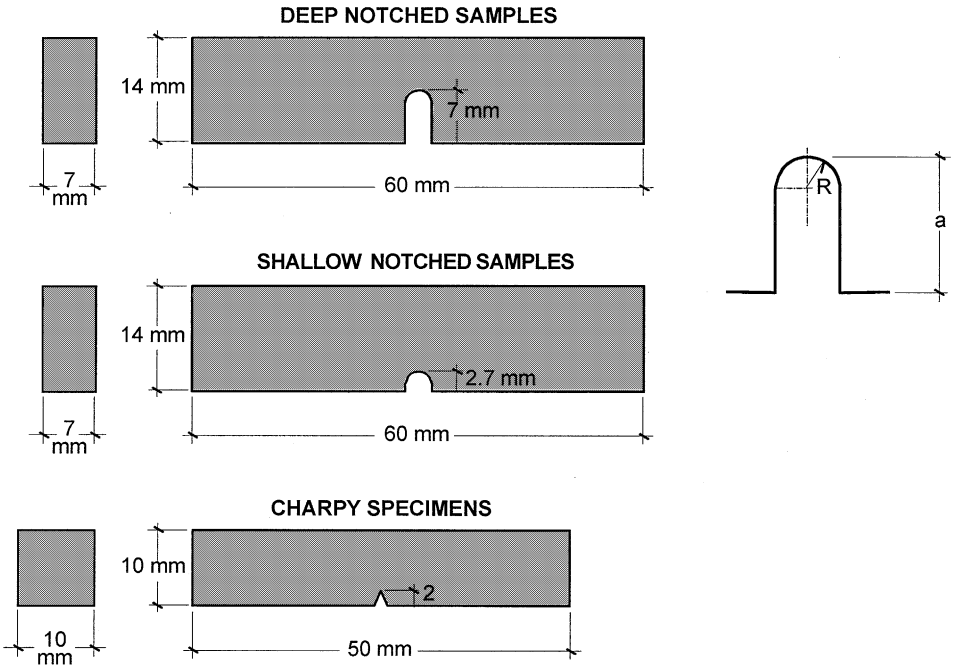

Fig. 22. Geometry of steel notched samples.

Table 5
Notch values of TPB specimens

Shallow notched beams		Deep notched beams	
R (mm)	a (mm)	R (mm)	a (mm)
0.096 ± 0.008	2.75 ± 0.09	0.101 ± 0.001	7.00 ± 0.30
0.170 ± 0.010	2.75 ± 0.02	0.171 ± 0.006	7.00 ± 0.20
0.500 ± 0.020	2.75 ± 0.01	0.505 ± 0.002	6.96 ± 0.04
		1.000 ± 0.010	6.96 ± 0.06

Errors correspond to 95% confidence interval.

Specimens were tested using the three point bend test technique under NOD control. Experimental results of load–NOD for the eight types of specimens are shown in Fig. 23. Each curve is the average value of four tests. All in all, 32 tests were performed.

The next step was to compute the load–NOD curves, for the eight geometries, using the process zone cohesive crack model, and to compare these results with the experimental ones.

The information needed to carry out these computations, apart from the sample geometry, was the softening function. Due to the small characteristic length of this steel, about 0.6 mm, the softening function was inferred using the indirect method because the size of the samples needed for the direct procedure was too small. The softening function used for this steel is depicted in Fig. 24. The material outside the process zone was modelled as an elastoplastic material with different behaviour in tension and compression (according to the data in Fig. 21).

Fig. 25 shows the comparison of peak loads from experimental results and numerical predictions based on the CCPZ model. The agreement is seen to be very good. Bars are used for experimental values; for each set of four tests the maximum, minimum, and average values are shown in the figure. Numerical values are shown as a continuous line. To account for the small differences in the notch length, as observed in the machined samples, two numerical predictions were done, each one corresponding to samples with notch lengths of $a \pm 0.04a$.

The behaviour of "cracked" samples, i.e., when $R = 0$, deserves some comments. Numerical predictions—using the CCPZ model and LEFM—are shown in the vertical axis as full triangles. Predictions

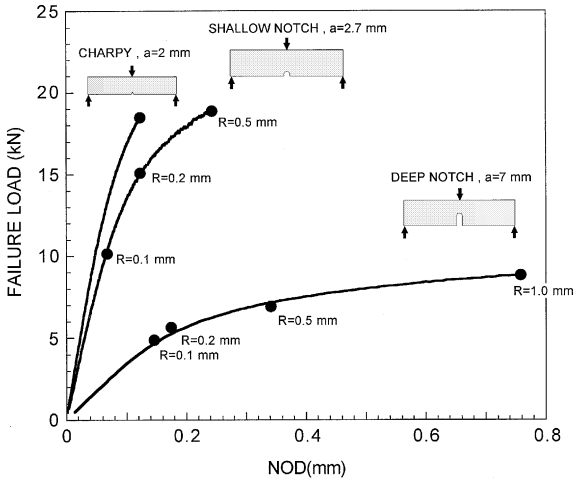

Fig. 23. Experimental results for notched steel samples (round points indicate the end of each test).

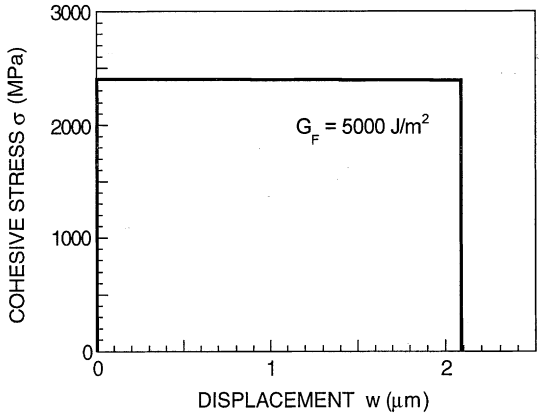

Fig. 24. Steel softening function.

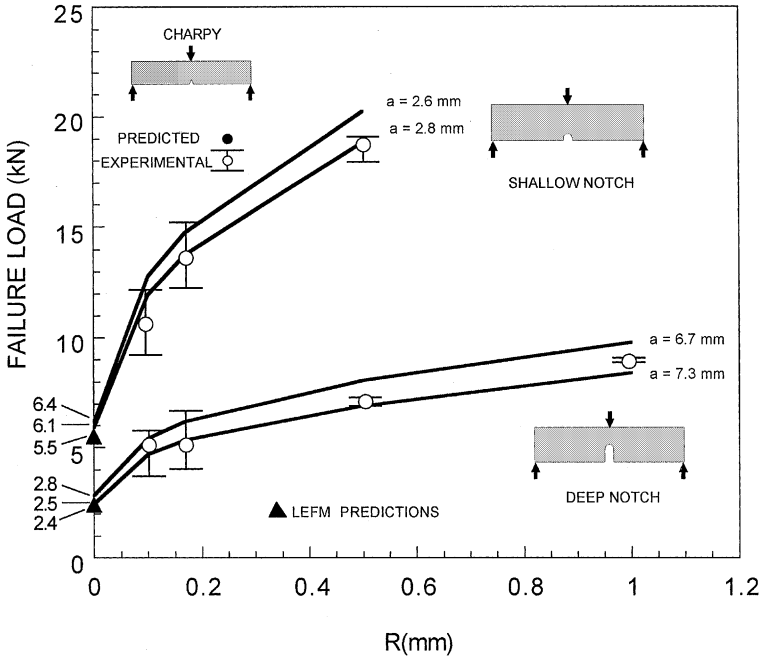

Fig. 25. Numerical predictions and experimental results of peak loads for TPB notched steel samples.

based on the CCPZ are always slightly higher than those based on LEFM. The reason is that for this particular material, the size of the fully developed cohesive zone and associated plastic zone is not negligible compared to the size of the beams tested.

As a further check of the suitability of the CCPZ model to reproduce experimental behaviour, sets of load–NOD curves were computed for all tested samples. Results are depicted in Fig. 26 for shallow and deep notched specimens as well as for the Charpy specimen. In each figure two experimental results are

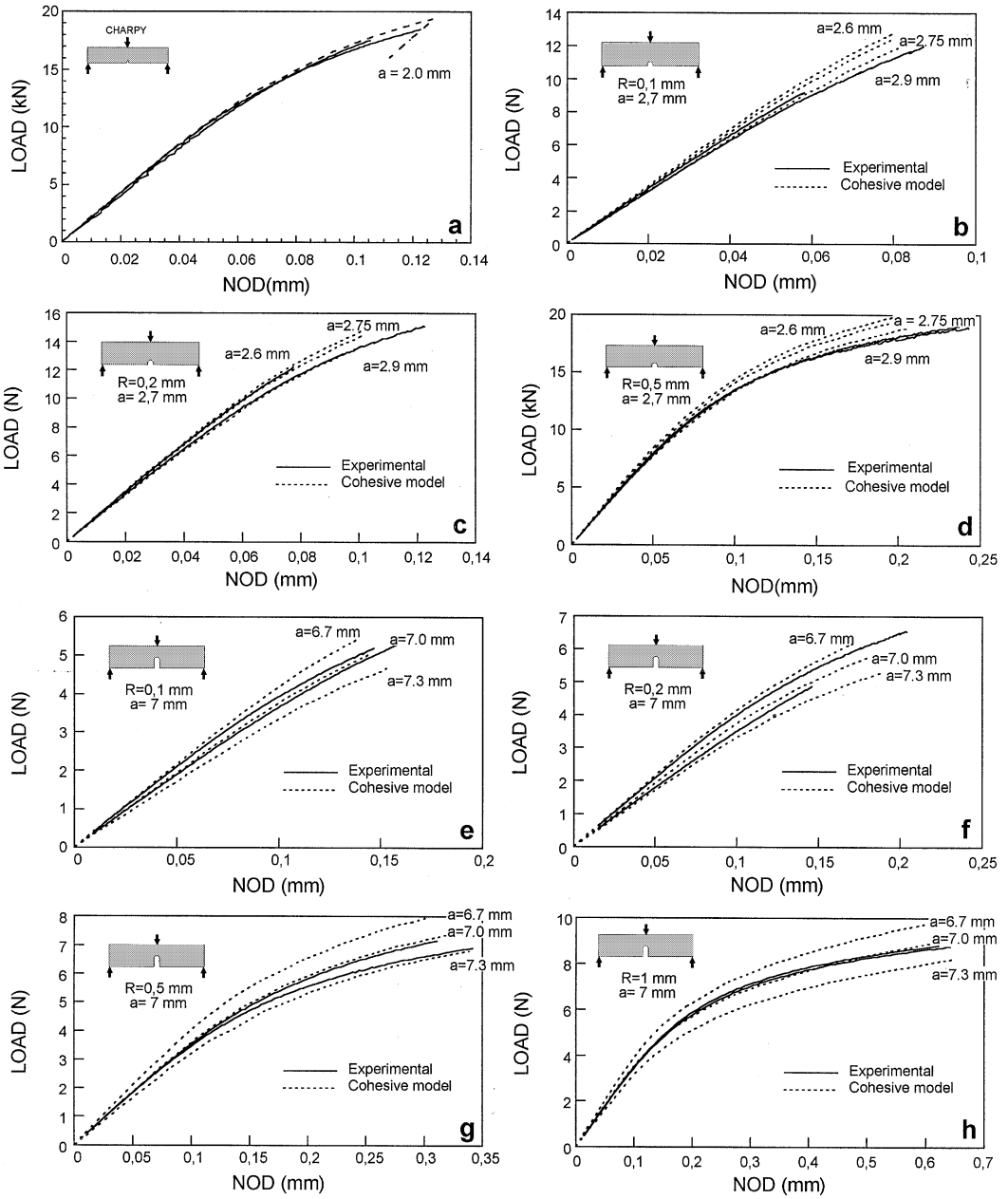

Fig. 26. Numerical predictions and experimental results of load–NOD curves for TPB notched steel samples.

shown (in continuous line) and a set of three numerical results for notched specimens are drawn (in dotted line), each one corresponding to beams with notches of $a - 0.04a$, a, and $a + 0.04a$, to take into account small notch differences during sample machining. For Charpy specimens only one numerical result for $a = 2$ mm was computed. Once more, the agreement between CCPZ predictions and experimental results is satisfactory.

Acknowledgements

The authors gratefully acknowledge financial support for this research provided by the Comision Interministerial de Ciencia y Tecnología (Spain) under grants MAT2000-1355 and MAT2000-1334.

References

[1] Aliabadi MH, Rooke DP. Numerical fracture mechanics. Dordrecht: Kluwer Academic Publishers; 1991.
[2] ASTM C 496. Standard test method for splitting tensile strength of cylindrical concrete specimens; 1990.
[3] Bazant ZP, Planas J. Fracture and size effect in concrete and other quasibrittle structures. Boca Raton, FL: CRC Press; 1998.
[4] Broberg KB. Cracks and fracture. San Diego, CA: Academic Press; 1999.
[5] Carpinteri A, editor. Nonlinear crack models for nonmetallic materials. Dordrecht: Kluwer Academic Publishers; 1999.
[6] Carpinteri A, Ferro G. Size effects on tensile fracture properties: a unified explanation based on disorder and fractality of concrete microstructure. Mater Struct 1994;27:563–71.
[7] CEB-FIP Model Code. Bulletín d'Information du CEB, 21; 1990.
[8] Cendon DA, Gálvez JC, Elices M, Planas J. Modeling the fracture of concrete under mixed loading. Int J Fract 2000;103:293–310.
[9] Elices M, Planas J. Fracture mechanics parameters of concrete: an overview. Adv Cement Based Mater 1996;4:116–27.
[10] Elices M, Guinea GV, Planas J. Measurement of the fracture energy using three-point bend tests. 3. Influence of cutting the P–δ tail. Mater Struct 1992;25:327–34.
[11] Elices M, Planas J, Guinea GV. Standard test method for determining fracture properties of concrete. Contribution to the ACI446 Committee on Fracture Toughness Test Standards; 2000.
[12] Elices M, Planas J, Guinea GV. Fracture mechanics applied to concrete. In: Fuentes M, et al., editors. Fracture mechanics: applications and challenges, ESIS publ. 26. Amesterdam: Elsevier; 2000. p. 183–210.
[13] Gálvez JC, Elices M, Guinea GV, Planas J. Crack trajectories under mixed mode and nonproportional loading. Int J Fract 1996;81:171–93.
[14] Gálvez JC, Elices M, Guinea GV, Planas J. Mixed mode fracture of concrete under proportional and nonproportional loading. Int J Fract 1998;94:267–84.
[15] Gálvez JC, Cendon DA, Planas J, Guinea GV, Elices M. Fracture of concrete under mixed loading. Experimental results and numerical prediction. In: Mihashi H, Rokugo K, editors. Fracture mechanics of concrete structures. Freiburg, Germany: Aedificatio Publishers; 1998. p. 729–38.
[16] Gómez FJ. Un Criterio de Rotura en Sólidos Entallados. PhD thesis. Dpt. Ciencia de Materiales, Universidad Politécnica de Madrid; 1998 (in Spanish).
[17] Gómez FJ, Elices M, Valiente A. Cracking in PMMA containing U-shaped notches. Fatigue Fract Engng Mater 2000;23:795–803.
[18] Guinea GV, Planas J, Elices M. Measurement of the fracture energy using three-point bend tests. 1. Influence of experimental procedures. Mater Struct 1992;25:212–8.
[19] Guinea GV, Planas J, Elices M. Correlation between the softening and the size effect curves. In: Mihashi H, Okamura H, Bazant ZP, editors. Size effect in concrete structures. London: E and FN Spon; 1994. p. 233–44.
[20] Guinea GV, Planas J, Elices M. A general bilinear fitting for the softening curve of concrete. Mater Struct 1994;27:99–105.
[21] Guinea GV, Pastor JY, Planas J, Elices M. Stress intensity factor, compliance and CMOD for a general three-point-bend beam. Int J Fract 1998;89:103–16.
[22] Guo Z, Zhang X. Investigation of complete stress-deformation curves for concrete in tension. ACI Mater J 1987;84:278–85.
[23] Hillerborg A, Modéer M, Petersson PE. Analysis of crack formation and crack growth in concrete by means of fracture mechanics and finite elements. Cement Concrete Res 1976;6:773–82.
[24] Hordijk DA. Local approach to fatigue of concrete. PhD thesis. Delft University of Technology, Delft, The Netherlands; 1991.
[25] Kitsutaka Y. Fracture parameters of concrete based on poly-linear approximation analysis of tension softening diagram. In: Wittmann FH, editor. Fracture mechanics of concrete structures, vol. 1. Freiburg, Germany: Aedificatio Publishers; 1995. p. 199–208.
[26] Kitsutaka Y. Fracture parameters by poly-linear tension softening analysis. J Engng Mech—ASCE 1997;123(5):444–50.
[27] Kitsutaka Y, Kamimura K, Nakamura S. Evaluation of aggregate properties on tension softening behaviour of high strength concrete. In: Malhotra VM, editor. High performance concrete. ACI SP149; 1994. p. 711–27.
[28] Kitsutaka Y, Kurihara N, Nakamura S. Evaluation method of tension softening properties. In: Kitsutaka Y, Mihashi H, editors. Proceedings of the FRAMCOS 3 Preconference Workshop on Quantitative Evaluation Methods for Toughness and softening Properties of Concrete, Gifu, Japan; 1998. p. 58–63.
[29] Li VC, Chang CM, Leung CKY. Experimental determination of the tension softening relations for cementitious composites. Cement Concrete Res 1987;17:441–52.

[30] Lin G, Heng XG, Cornec A, Schwalbe KH. The effect of strength mis-match on mechanical performance of weld joints. Int J Fract 1999;96:37–54.
[31] Mihashi H. Material structure and tension softening properties of concrete. In: Bazant ZP, editor. Fracture mechanics of concrete structures. London: Elsevier Applied Science; 1992. p. 239–50.
[32] Neville AM. Properties of concrete. London: Pitman; 1981.
[33] Petersson PE. Crack growth and development of fracture zone in plain concrete and similar materials. Report TVBM-1006, Div. of Building Mat, Lund Institute of Technology, Sweden; 1981.
[34] Philips DV, Binsheng Z. Direct tension tests on notched and unnotched plain concrete specimens. Mag Concrete Res 1993;45: 25–35.
[35] Planas J, Elices M. Towards a measure of GF: an analysis of experimental results. In: Wittmann FH, editor. Fracture toughness and fracture energy of concrete. Amsterdam: Elsevier; 1986. p. 381–90.
[36] Planas J, Elices M. Nonlinear fracture of cohesive materials. Int J Fract 1991;51:139–57.
[37] Planas J, Elices M. Shrinkage eigenstresses and structural size-effect. In: Bazant ZP, editor. Fracture mechanics of concrete structures. London: Elsevier Applied Science; 1992. p. 939–50.
[38] Planas J, Elices M. Asymptotic analysis of a cohesive crack. 1. Theoretical background. Int J Fract 1992;55:153–77.
[39] Planas J, Elices M. Asymptotic analysis of a cohesive crack. 2. Influence of the softening curve. Int J Fract 1993;55:221–37.
[40] Planas J, Elices M, Guinea GV. Measurement of the fracture energy using three-point bend tests. 2. Influence of bulk energy dissipation. Mater Struct 1992;25:305–12.
[41] Planas J, Guinea GV, Elices M. Rupture modulus and fracture properties of concrete. In: Wittmann FH, editor. Fracture mechanics of concrete structures, vol. 1. Freiburg, Germany: Aedificatio Publishers; 1995. p. 95–110.
[42] Planas J, Guinea GV, Elices M. Generalized size effect equation for quasibrittle materials. Fatigue Fract Engng Mater 1997;20(5):671–87.
[43] Planas J, Guinea GV, Elices M. Size effect and inverse analysis in concrete fracture. Int J Fract 1999;95:367–78.
[44] Planas J, Guinea GV, Elices M. Integral equation method for modelling cracking in concrete. Computational fracture mechanics in concrete tecnology. Southampton, UK: WIT Press/Computational Mechanics Publications; 1999. p. 103–32 [chapter 4].
[45] RILEM-Recommendation (TC50-FMC). Determination of fracture energy of mortar and concrete by means of three-point bent test on notched beams. Mater Struct 1985;18:285–90.
[46] Rocco C. Influencia del Tamaño y Mecanismos de Rotura del Ensayo de Compresión Diametral. PhD thesis. Dpt. Ciencia de Materiales, Universidad Politécnica de Madrid; 1996 (in Spanish).
[47] Rocco C, Guinea GV, Planas J, Elices M. Size effect and boundary conditions in the Brazilian test: experimental verification. Mater Struct 1999;32:210–7.
[48] Roelfstra PE, Wittmann FH. Numerical method to link strain softening with failure of concrete. In: Wittmann FH, editor. Fracture toughness and fracture energy of concrete. Amsterdam: Elsevier Science; 1986. p. 163–75.
[49] Rots J. Computational modeling of concrete fracture. PhD thesis. Delft University of Technology, Delft, The Netherlands; 1988.
[50] Tijssens MGA, van der Giessen E, Sluys LJ. Modeling of crazing using cohesive surface methodology. Mech Mater 2000;32:19–35.
[51] Uchida Y, Kurihara N, Rokugo K, Koyanagi W. Determination of tension softening diagrams of various kind of concrete by means of numerical analysis. In: Wittmann FH, editor. Fracture mechanics of concrete structures, vol. 1. Freiburg, Germany: Aedificatio Publishers; 1995. p. 17–30.
[52] Ulfkjaer JP, Brincker R. Indirect determination of the σ–w relation of HSC through three point bending. In: Rossmanith HP, editor. Fracture and damage of concrete and rock. London: E and FN Spon; 1993. p. 135–44.
[53] Valiente A, Elices M. Premature failure of prestressed steel bars. Engng Failure Anal 1998;5:219–27.
[54] van Mier JGM, Vervuut A. Micromechanical analysis and experimental verification of boundary rotation effects in uniaxial tension tests on concrete. In: Baker G, Karihaloo BL, editors. Fracture of brittle disordered materials: concrete, rock and ceramics. London: E and FN Spoon; 1995. p. 406–20.